Article

# Elucidation of Local Ordering and Atomic-Scale Structure in Polymer-Derived SiOC

Haira G. Hackbarth, Thomas S. Key, Taren Cataldo, Ian Dillingham, Yuwei Yang, Matthew B. Dickerson,* Timothy L. Pruyn,* and Nicholas M. Bedford*

Read Online

| ACCESS | Metrics & More | Article Recommendations | Supporting Information |

**ABSTRACT:** Silicon oxycarbide (SiOC) is a versatile ceramic material with tunable microstructure and compositions that can be modulated through precursor chemistry and processing conditions. Though there are several noteworthy uses of SiOC across a range of application spaces, the difficulties in elucidating the short- to medium-range order within these materials have limited the maturation of strategies to precisely control $SiC_xO_{4-x}$ compositions for user-tailored applications. In this contribution, we implement a range of synchrotron scattering and spectroscopy methods coupled with stochastic modeling techniques to elucidate changes in local chemistry and structure associated with the pyrolysis of a commercially available SiOC polymer precursor. Stochastic modeling approaches provide valuable insights into decoupling local Si−O and Si−C environments while confirming predominate heterogeneous phases in

materials. Using pyrolysis temperatures between 250 to 800 °C results in a heterogeneous material predominately composed of SiOC and amorphous $SiO_2$ domains. At 1100 °C, redistribution of Si−C pairs in the SiOC network and Si−O from the $SiO_2$ domains create a more ordered SiOC phase with local cubic SiC-like ordering. In addition, residual carbon leads to a detectable carbon phases at 1100 °C that persist at higher temperatures. These efforts address the difficulties of obtaining atomic-scale insights into the local structure and nanoscale heterogeneities in SiOC, providing pathways toward establishing structure−property relationships for future materials development.
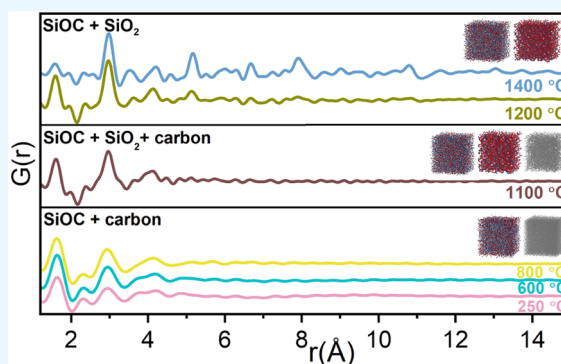
## 1. INTRODUCTION

Silicon oxycarbides (SiOCs) are a versatile class of ceramics used for a range of applications, such as fiber reinforced composites,[1] catalyst supports,[2] electrodes in lithium-ion batteries,[3] sensors,[4] medical devices,[5] and gas storage media.[6] Their versatility arises from the ability to tune composition and microstructure while being inexpensive and straightforward to process. Most commonly, SiOCs are made through sol−gel chemistry,[7,8] and more recently, polymer-derived methods.[9–12] From a synthetic point of view, the potential to modify the coordination environment of SiOCs through initial chemistry and control of processing conditions is especially attractive.[11,13] For instance, changes in the pyrolysis atmosphere using reactive species, such as $H_2$, $H_2O$, or $CO_2$, have been shown to influence the final phases of polymer-derived SiOCs.[14,15] Similarly, adjusting the initial carbon content in the precursor by incorporating C-rich cross-linking agents (e.g., Si−CH=CH2) or modifying functionalization of polysiloxanes further enhances the electrical conductivity and thermal stability of SiOCs.[16,17] These attractive properties are attributed to the unique SiOC molecular architecture, which is derived from local structure and nanoscale heterogeneities.[8,10,11] The structure around Si atoms within SiOC can

be described as $SiC_xO_{4-x}$ tetrahedra, where variations in C and O can progressively evolve depending on both precursor chemistry and synthetic conditions throughout the various stages of processing.[18–20] Attaining greater insights into the short- to medium-range order within these materials may enable more precise design SiOC compositions[13,20,21] and providing new strategies for the directed design of SiOC with user-defined properties.

SiOCs are predominantly disordered materials that can resist crystallization up to 1500 °C, making their characterization via traditional crystallographic methods difficult.[7,13,21,22] The light atomic mass and relative similarities between Si, O, and C further complicate straightforward characterization, especially as variations in C- and O-containing phases are anticipated upon pyrolysis.[20,21] For these reasons, the atomic structure and phase evolution involved in the SiOC formation remains

largely ambiguous. Insights into understanding local SiOC structure has been pursued using solid-state [29]Si and ^{13}C nuclear magnetic resonance (NMR), X-ray diffraction (XRD), and high-resolution transmission electron microscopy (HR-TEM).[9,23,24] It is reasonable to conclude that the atomic structure of the glassy phase influences the final ceramic pyrolyzed at higher temperatures. ^{29}Si NMR studies have shown continuous interpenetrating phases of O-rich units ($SiO_xC_{4-x}$, $x \geq 2$) and carbon, where C-rich ($SiO_xC_{4-x}$, $x < 2$) is located in the interface with the free carbon nanodomains,[9,23] while other studies suggest nanoscale domains of either $sp^2$ C or $SiO_2$ domains present in a larger matrix of the corresponding comaterial.[25,26] At higher pyrolysis temperatures, many studies propose that the formation of SiOC glassy material through to ~1100 °C, which then phase segregates into $SiO_2$, SiC, and/or C phases of varying crystallinity at higher pyrolysis temperatures.[7,24,27] While acknowledging the differences in pyrolysis conditions and SiOC precursors implemented in each individual study makes cross comparisons difficult, the lack of even residual SiOC phases at higher temperatures at the cost of SiC and $SiO_2$ domains is curious. Indeed, recent work by Lu and Cheney using high-energy X-ray diffraction (HE-XRD) measurements and reactive force field simulations showcase an SiOC network in materials pyrolyzed at higher temperatures.[21]

In this paper, we investigate the changes in the local structure of polymer-derived SiOCs using a range of synchrotron scattering and spectroscopy data sets.[28,29] For our study, a commercially available polysiloxane was pyrolyzed at temperatures ranging from 250 to 1400 °C. This precursor was chosen due to its exceptional thermal and oxidative resistance in SiOC-based nanocomposites and the limited amount of structural information known about polymer-derived SiOCs. Here, we combined atomic pair distribution function (PDF) analysis of HE-XRD data sets with element-specific insights from X-ray absorption spectroscopy (XAS) and other characterization tools to better understand the local structure of SiOCs as a function of pyrolysis temperature. As PDF uses both Bragg peaks and diffuse scattering, the method is ideal for obtaining structural atomic-scale structural information that cannot readily be ascertained via traditional diffraction techniques.[28] To address the nanoscale heterogeneities in SiOCs, mesoscopic reverse Monte Carlo (RMC) simulations were performed to more accurately reflect different phases in the material.[30] The combined results show that pyrolysis at 250 to 800 °C results in a heterogeneous material composed of a mix of poorly ordered SiOC and $SiO_2$ domains. For materials pyrolyzed at 1100 to 1400 °C, segregated carbon was detected in addition to the predominant SiOC phase. Despite increased local ordering between 1200 and 1400 °C, the final SiOC retains its distorted structure. This work addresses a major gap in experimental methodologies for characterizing polymer-derived SiOCs and provides new insights into atomic evolution of SiOCs that can be used to help design processing protocols for materials with user-defined properties.

## 2. EXPERIMENTAL METHODS

**2.1. PDC Processing.** A commercial liquid polycarbosiloxane, precursor for silicon oxycarbide (SiOC) ceramics, (Polyramic SPR-036, Starfire Systems) was purchased and used as received. To induce cross-linking in the SiOC precursor, a controlled thermal treatment was conducted under vacuum conditions. The precursor was heated at a rate of 1 °C/min and held for 1 h at 160 and 250 °C successively. Subsequently, pyrolysis was executed under a continuous flow of argon at varying temperatures for 1 h, employing a ramp rate of 1 °C/min. The pyrolysis process took place within an alumina ($Al_2O_3$) tube containing a graphite sleeve, with final pyrolysis temperatures ranging from 400 to 1400 °C. Post pyrolysis, the samples were allowed to cool within the furnace over a period of approximately 8 h. The pyrolyzed materials were ground into powders using a mortar and pestle, ensuring a finely homogenized material suitable for subsequent characterization.

**2.2. Materials Characterization.** *2.2.1. Raman Spectroscopy.* Raman spectroscopy was conducted on a Renishaw inVia Raman microscope with an excitation wavelength of 514.5 nm line, an Ar-ion laser as the excitation source, and a 1800 L/mm grating. The spectral measurements were taken in an extended mode in a range from 500 to 3200 cm$^{-1}$. Gaussian curve fitting was performed using OriginPro software package, $I_{(D)}/I_{(G)}$ intensity ratios were extracted from the obtained areas, and the size of the clusters ($L_a$) was estimated according to the relation: $L_a = 4.4 \times (I_D/I_G) - 1$ nm.[31] Raman shifts were only detected on high-temperature processing materials from 1100 to 1400 °C.

*2.2.2. Attenuated Total Reflectance Fourier Transform Infrared (ATR-FTIR).* ATR-FTIR were acquired using a PerkinElmer series 400 ATR-FTIR spectrometer in the 450–4000 cm$^{-1}$ wavenumber range. A resolution of 4 cm$^{-1}$ and a total of 64 scans per spectrum were imposed.

*2.2.3. X-ray Absorption Near-Edge Structure (XANES).* XANES measurements at the Si K-edge were performed at the SXRMB beamline of the Canadian light source. The powders were dispersed onto carbon tape for the measurement. Data was collected from ~30 eV below to ~80 eV past the Si K-edge (1838.9 eV) using a seven-element Si-drift detector (SDD) in both fluorescence yield (FY) and total electron yield (TEY) modes. Only the FY spectra are presented in the manuscript, to provide bulk information. Data processing was performed using Demeter XAS software package.[32]

*2.2.4. Near-Edge X-ray Absorption Fine Structure (NEXAFS).* NEXAFS measurements were performed at the C (280–320 eV) K-edge using the SXR beamline of the Australian Synchrotron. The powdered samples were pressed onto copper (Cu) tape for analysis. The NEXAFS data were recorded in partial electron yield (PEY) mode at an angle of 55° between the incoming irradiation and the sample surface. The data were normalized by the incident photon flux $I_0$ monitored using an Au grid with partial transmissivity positioned before the sample. A photodiode was used in all C K-edge measurements as a secondary normalization reference to remove carbon from the upstream optics in the measured carbon spectra. The C K-edge peaks in the NEXAFS spectra were decomposed into Gaussian peaks using the semiautomated peak fitting methods in QANT in Igor Pro.[33] The C K-edge spectra were fit with five main peaks around 285.28, 287.4, 288.31, 291.38, and 298.83 eV.

*2.2.5. High-Energy X-ray Diffraction (HE-XRD).* HE-XRD measurements were performed at the 11-ID-C beamline (Advanced Photon Source, Argonne National Laboratory). The powder samples were loaded into Kapton capillaries, and diffraction patterns were collected using 115.05 keV (wavelength 0.108 Å irradiation with a $Q_{max}$ of 28.0 Å). The scattering images were converted into one-dimensional plot
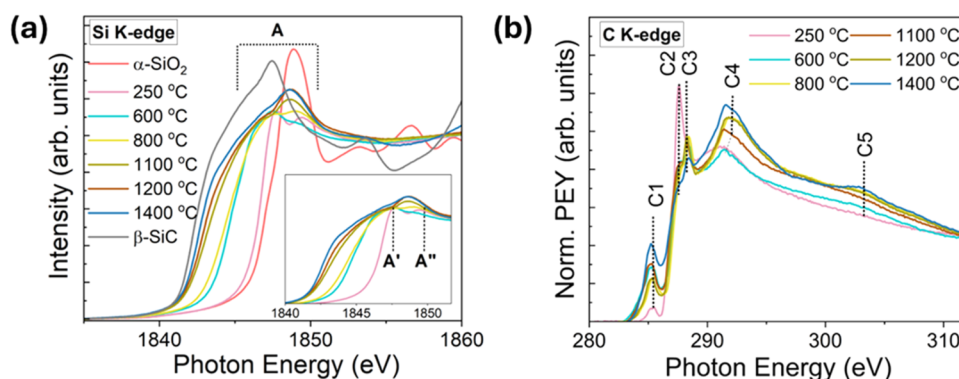
**Figure 1.** (a) Si K-edge XANES spectra of pyrolyzed materials, including reference materials $\alpha$-SiO$_2$ and $\beta$-SiC. NEXAFS spectra at (b) C K-edge.

using Fit2D software,[34] employing CeO$_2$ as a calibration standard to determine sample-to-detector distance. PDFs were calculated using PDFgetX3,[35] where HE-XRD patterns were background corrected against an empty X-ray capillary, converted into reduced structure functions, and Fourier transformed into their corresponding atomic PDFs.

**2.3. Reverse Monte Carlo (RMC) Structure Modeling.** RMC simulations were performed on the PDFs of ceramics pyrolyzed at 250, 600, 800, 1100, 1200, and 1400 °C using the fullrmc program.[36] To generate our initial SiOC configuration, we used a builder tool integrated within the same platform.[37,38] For that, an amorphous cubic structure was built encompassing a diameter of ~50 Å, containing a total of 8045 atoms. The initial configuration was composed of 49.13% Si, 24.43% O, and 26.44% C, with stoichiometry constrained based on reported elemental composition of SiOC derived from a Polyramic resin (Starfire systems).[11] The nearest-neighbor distances were obtained from previously published studies on SiOCs: 1.6 Å for Si—O, 1.86 Å for Si—C, 3.31 Å for C—C, 2.55 Å for O—O, and 3.11 Å for Si—Si.[19,22] All RMC simulations incorporated a random translation movement on selected atoms in any direction with an amplitude up to 0.1 Å under nonperiodic boundary conditions. Coordination constraints to describe the nearest-neighbor environments were also introduced into the RMC model, imposing the closest approach to 1.5 Å. At each move, the $\chi^2$ difference between the experimental PDF and the simulated PDF was calculated, over the ranges from 1.2 to 12 Å. To assess stoichiometric variations in the resulting SiOC configurations, we implemented an atom removal generator step using the RemoveGenerator feature in fullRMC.[37,39] Subsequently, the heterogeneities associated with the pyrolysis of polymer-derived SiOCs were explored using a mesoscopic modeling tool,[30,37] where configurations of the SiO$_2$[40] and graphite[41] crystal structures were implemented depending on the processing temperature. For materials pyrolyzed between 250 and 800 °C, we used a combination of SiOC and SiO$_2$ starting configurations. At 1100 °C, a three-configuration system was tested, including an additional graphite structure. Then, for temperatures exceeding 1200 °C, the mesoscopic calculations included a combination of SiOC and graphite configurations. Finally, we investigated the potential presence of SiC phases in materials obtained from 1100 to 1400 °C, incorporating a $\beta$-SiC structure into our calculations.[30] Due to amorphous nature of the structures investigated, all simulations were performed under nonperiodic boundary conditions, applying a shape function to compensate for density loss.[38] Note that all

mesoscopic simulations started with equal contributions of each phase and were permitted to change using fullRMC's mesoscopic multiframe option.[37] Coordination number (CN) and bond angle distribution parameters were extracted from the SiOC RMC-generated structures using OVITO[42,43] and ISAACS,[44] respectively.

## 3. RESULTS AND DISCUSSION

SPR-036 is a commercially available polysiloxane and is used as a SiOC precursor in this study due to its wide use in research and industry settings. Previous studies demonstrate that SPR-036 converts into an amorphous SiOC network upon thermal degradation of Si—H and/or Si-CH$_3$ moieties present in the polymer precursor (400−800 °C), followed by ceramization reactions above 1000 °C.[45,46] Despite growing applications using polysiloxane, such as SPR-036 as SiOC precursors,[45,47,48] there is a considerable lack of fundamental structural information regarding the formation of SiOCs from preceramic polymers. To elucidate the evolution of SiOC structure at the atomic scale, materials derived from pyrolysis of SPR-036 at a range of temperature (250 to 1400 °C) were analyzed in depth.

Element-specific local structure and chemistry was obtained from X-ray absorption spectroscopy (XAS) at the Si and C K-edges. Si K-edge spectra (Figure 1(a)) exhibit absorption profiles found in both fully coordinated Si—C and Si—O transitions, as expected in SiOC structures.[49−52] The main absorption feature, labeled as "**A**", is assigned to the electronic transition from Si 1s core level into a Si 3p-like unoccupied electronic state.[52,53] Figure 1(a) shows profound changes in the Si K-edge spectra as the pyrolysis progressed, reflected in the energy position and shape profile. In particular, at lower processing temperatures (250 to 800 °C) variations in **A** came in the form of a doublet profile (**A′** and **A″**). The ratio of this doublet has been previously linked to different C/O stoichiometries in polymeric SiO$_x$C$_y$H$_z$, where a pronounced **A′** is found in C-rich systems within a predominant Si—C environment.[52] At 250 °C, the energy position of the rising edge aligns closely with that of the $\alpha$-SiO$_2$ reference compound, indicating a predominant local Si—O bonding environment.[47] In addition, we observed a pronounced doublet profile at 250 °C, which is likely attributed to the polymeric Si—C environment still present at 250 °C.[47,52] Pyrolysis at 600 and 800 °C leads to noticeable shifts in the energy position of the rising edge as due to a presumed increase in neighboring carbon atoms. Note that at this temperature range, redistribution reactions of Si—H and/or Si-
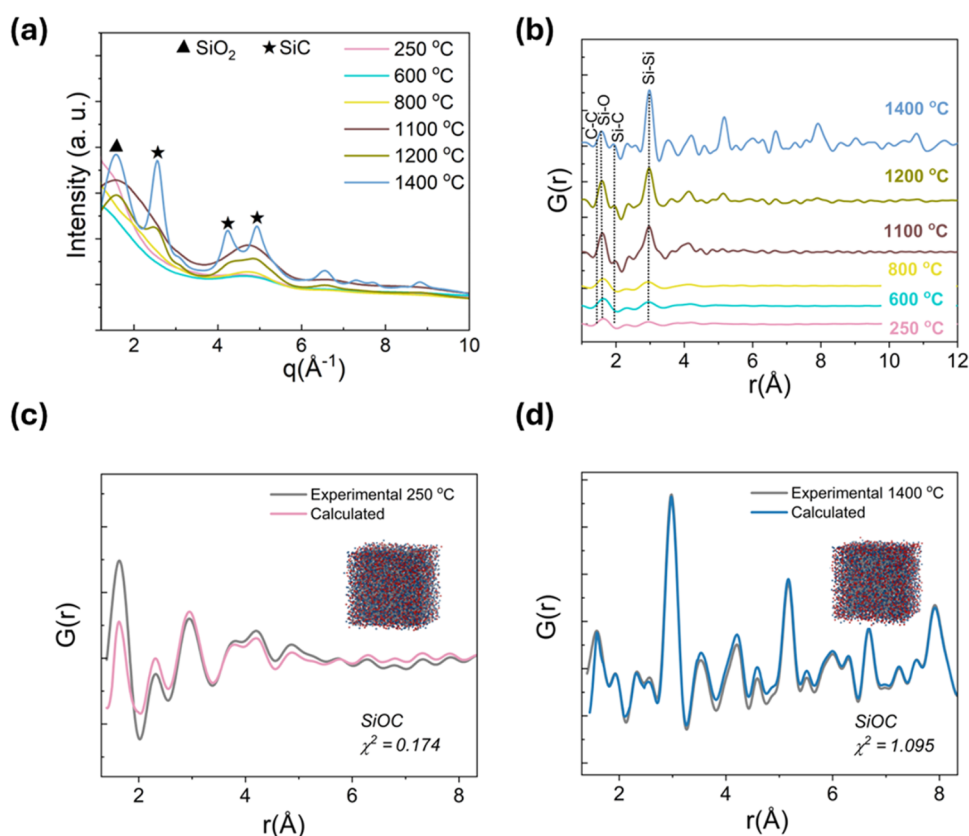
**Figure 2.** (a) HE-XRD patterns of SPR-036 pyrolyzed at selected processing temperatures in ranges up to 10 Å$^{-1}$. (b) Atomic PDFs at selected temperatures up to 12 Å. RMC-generated fittings using a single-phase SiOC configuration at selected temperatures of (c) 250 °C and (d) 1400 °C.

CH$_3$ are expected to take place.[45,46] Further pyrolysis at 1100 to 1400 °C shifts the energy position to lower energy, approaching the Si K-edge of a reference $\beta$-SiC. This energy shift can be attributed to the lower electronegativity polarization of Si−C compared to Si−O bonding.[52,53] As a general trend, materials obtained from 1100 to 1400 °C exhibit a broad main peak with similar onset energy of Si−C and white line intensity of Si−O, confirming the mixed Si−C and Si−O bonding environment.[50,54] The apparent shoulder in the spectra suggests the presence of distinct SiOC$_3$, SiO$_2$C$_2$, and SiO$_3$C groups derived from the formation of the SiOC network,[55] forming local domains similar to those characterized in previous $^{29}$SI NMR studies.[9,23,56]

C K-edge near-edge X-ray absorption fine structure (NEXAFS) spectra and associated peak fitting results are depicted in Figures 1(b) and S1, respectively. Here, NEXAFS was employed to better understand the polymer-to-ceramic transformation, especially in the context of C-rich phase. Broadly, it is important to note that in polymer-derived SiOC, C atoms can be either integrated into the SiOC network with sp$^3$ hybridization (Si−C, such as in $\beta$-SiC) or as a graphitic C phase with sp$^2$ hybridization.[13] The C K-edge spectra display a sharp peak at 285.28 eV (**C1**), corresponding to unsaturated in $\pi^*$ sp$^2$ C contributions.[49,50,57] Further analysis of **C1**, shown in Figure S1(a), clearly demonstrates that pyrolysis from 1100 to 1400 °C has a great influence on the sp$^2$-like character of ceramics, likely due to segregated graphite-like formations.[30] An opposite trend was observed in the intensity of the feature at 287.4 eV (**C2**), which corresponds to the 1s → $\sigma^*$ transition of C−H bonds (Figure S1(b)).[50,51,58] Beyond 250 °C, this feature is significantly reduced, likely due to the thermal

liberation of Si−CH$_3$ species at higher temperatures.[47] The feature at 288.31 eV (**C3**) arises from carbonyl groups that are likely on the surface during Si−O−C network formation through the possible oxidation of surface graphite.[58] The subsequent features **C4** and **C5** are assigned to dipole transitions from the C 1s orbitals to $\sigma^*$-character bands formed by the sp$^3$-hybridization of C orbitals tetrahedrally coordinated with Si atoms.[30,57] Our results reveal an increase of the sp$^3$ character of C species upon pyrolysis, which was readily noticeable at temperatures above 800 °C due to Si−O−C ceramization.

Raman spectroscopy (Figure S2) was performed on SiOCs to complement our C K-edge measurements for SiOCs pyrolyzed at higher temperatures to better understand the nature of graphite-like phases. Our results indicate the presence of sp$^2$ C domains in the SiOC, with characteristic D and G bands at 1355 and 1600 cm$^{-1}$, respectively.[59] The D band refers to disorder-induced double resonance from in-place vibrations of aromatic rings with A$_{1g}$ symmetry, whereas the G band is from in-plane stretching vibration E$_{2g}$ mode of sp$^2$ C atoms.[13,45,60,61] In all cases, a second-order D + G band at 2902 cm$^{-1}$ was detected in our materials, which is attributable to a two-phonon process involving D and G phonons.[16,60] At 1100 °C, the D and G bands were broad and overlapped, indicating a highly disordered and defective C environment.[16,62,63] Subsequent pyrolysis at 1200 and 1400 °C results in a narrow and distinct D and G bands, which have been previously associated with a decrease of defect sites and structure disorder.[16,60] Furthermore, the D + G band becomes more pronounced within an additional 2D band observed at these temperatures. Although the latter is usually found in

defect-free graphite, the persistent broadness of the D + G band, as well as absence of G′ band, suggests a defective C environment.[13,59,62] To further verify the degree of graphitization of carbon phases, we estimated the $I_D/I_G$ ratio from Raman spectra, as shown in Figure S2(e). Although an unexpected increase in the $I_D/I_G$ ratio was noted from 1100 to 1200 °C, previous findings associate this to the critical phase changes during microstructure evolution from disordered carbon to defective graphite-like configuration.[63] In contrast, at 1400 °C, the decrease in the $I_D/I_G$ ratio confirms the graphitization of nanoscale carbon structures.[59] The further estimation of the lateral crystal size ($L_a$), shown in Figure S2(f), reveals that the carbon domain increases from 1.97 to 2.29 nm at 1100 and 1400 °C, respectively. These combined results corroborate with the trends observed in C K-edge NEXAFS analysis (Supporting Figure S1(a)).

Figure S3 displays the Fourier transform infrared (FTIR) spectroscopy performed on SiOCs to provide further chemical insights into key change that occurred after pyrolysis. At processing temperatures between 250 and 600 °C, organic silyl groups were detected due to the presence of preceramic polymer species. These signals were expected due to redistribution reactions of Si−H and/or Si−CH$_3$ moieties present in the precursor from 250 to 600 °C.[45,46] Specifically, at this temperature range, the FTIR spectra exhibit peaks assigned to vibrations of C−H stretching in the CH$_3$ side group (at 2900 cm$^{-1}$), Si−H bond (at 2120 cm$^{-1}$), Si−C bending of Si−CH$_3$ bond (at 1250 cm$^{-1}$), Si-CH$_2$−CH≡CH$_2$ deformation (within the range of 1630−1640 cm$^{-1}$), and the Si−C stretching of side groups (around 800 cm$^{-1}$).[47,64] Materials pyrolyzed from 800 to 1400 °C exhibit almost similar FTIR spectra, dominated by two main features at 810 and 1050 cm$^{-1}$, corresponding to the Si−C and asymmetric O stretching in Si−O−Si bridges, respectively.[45,65] In the latter, a pronounced shift was observed from 800 to 1100 °C, indicating more ordered bridging angles due to the onset of SiOC network formation upon ceramization.[45,65]

To investigate the structural coherence of the polymer-derived SiOCs, HE-XRD was performed on materials pyrolyzed from 250 to 1400 °C (Figure S4(a)). HE-XRD patterns corresponding to the temperatures with pronounced phase transformations were selected for detailed analysis and are shown in Figure 2(a). From 250 to 1100 °C, all materials display diffuse features and broad Bragg-like peaks consist with poorly ordered SiOCs. Materials pyrolyzed at 1200 and 1400 °C begin to show more definable Bragg peaks arising from the onset of crystallization, consistent with our previous characterization. The peak at 1.86 Å$^{-1}$ aligns with the 101 reflection of $\alpha$-SiO$_2$,[66] where peaks beyond ~2.5 Å$^{-1}$ correspond to SiC reflections.[16,27,30] There is a notable shoulder peak at 3.15 Å$^{-1}$ corresponding to the graphite-like phase as well as that is most prevalent at 1400 °C.[19] The lower q-space feature that manifest themselves at lower temperatures suggest that an earlier onset of Si−O network formation occurs prior to the ordering of the Si−C-like phase at higher q-space. A similar trend was observed in a recent work of Doan-Nguyen et al. and Lu and Chaney in the ceramization of polysiloxanes.[21,66] It is crucial to note that even at higher temperatures, the materials lack long-range structural order and that the indexing of possible Bragg peaks, while insightful, may not directly indicate appreciate phase separation. Rather, given the highly diffuse nature of the HE-XRD pattern overall, localized clusters of

SiO$_{4−x}$C$_x$ likely adapt SiC-like phases with mixtures of local O and C coordination around the Si atoms, as discussed below.

Atomic PDFs were then generated from HE-XRD patterns to better understand atomic-scale structural of SiOCs given the limited structural coherence is present in these materials (Figure S4(c)). Figure 2(b) shows atomic PDFs obtained at selected temperatures, ranging from 250 to 1400 °C. From 250 to 1100 °C, a rapid decay of the atomic pairs begins at ~5 Å, implying a lack of longer-range ordering beyond this distance. Several peaks emerged in the 5 to 12 Å range upon pyrolysis at 1200 to 1400 °C due to medium-range ordering of ceramics. The PDFs shown in Figure 2(b) exhibit prominent contributions from Si−O and C−C, and Si−C first coordination spheres, located from 1.6 to 1.92 Å.[19,22,67−71] Subsequent peaks at 2.36 and 2.58 Å were assigned to C−C and O−O distances in the second coordination shell.[19,22,67−70] The strong peak at ~3.1 Å corresponds to the distance between two Si atoms in adjacent SiC$_x$O$_{4−x}$ tetrahedral units.[71] From 250 to 800 °C, Si−O, O−O, and Si−Si atomic contributions dominate the PDFs. Note that the first broad peak at ~1.6 Å may contain overlapped contributions from the first nearest-neighbor Si−O and C−C distances as well. Clearly, changes in the local structure were observed in the PDFs of SiOCs obtained in the temperature range of 1100 to 1400 °C. In particular, both Si−O and Si−C interatomic distances become shorter upon pyrolysis, indicating structural changes in SiO$_x$C$_{4−x}$ tetrahedral units.[30,69] In contrast, the Si−O atomic pairs were suppressed at this temperature range, consistent with Si K-edge measurements. We also noted that Si−C atomic pairs become more pronounced at >1100 °C. At high processing temperatures (1200−1400 °C), ceramics exhibit a distinct peak at 3.53 Å, corresponding to the second nearest-neighbor Si−C bond distances and/or the fourth nearest-neighbor C−C bond distances.[20,72] Taken together, the PDF data sets suggest that the formation of the SiOC network is likely to occur through the expense of oxygen-rich tetrahedral (e.g., SiO$_4$/SiO$_3$C).[19]

RMC simulations of the PDF data sets were then used to construct atomic-scale models of SiOCs, providing insights into local ordering that would be difficult to obtain otherwise.[28,29,73] As described in the Supporting Information, we started our investigations using a single SiOC phase as the initial configuration containing Si, O, and C atoms. This starting configuration represents the structure of a SiOC network where Si is randomly coordinated with O and C atoms. The resulting fits implementing a single-phase SiOC network are shown in Figure S5 and Table S1. Compared with the experimental PDFs, a decreased intensity was observed in the first coordination peak of the RMC fittings, particularly between 250 and 800 °C (Figures 2(c) and S5) where the single-phase model had trouble fitting the first Si−O/C coordination sphere. This effect was less pronounced at subsequent temperatures, as shown in Figure 2(d), which corresponds to the RMC fitting at 1400 °C. This initial attempt of using RMC showcase that SiOCs pyrolyzed at high temperatures can be mostly captured by a randomized Si−O/C model, and it does not capture some of the complexities in polymer-derived SiOCs made at lower temperatures. This could be due to local SiO$_2$ formations, as suggested by Si K-edge measurements and HE-XRD observations, and/or remnant polymeric functionalities.

As a first step to better understand heterogeneity and changes to SiOC stoichiometry, a defective generator was
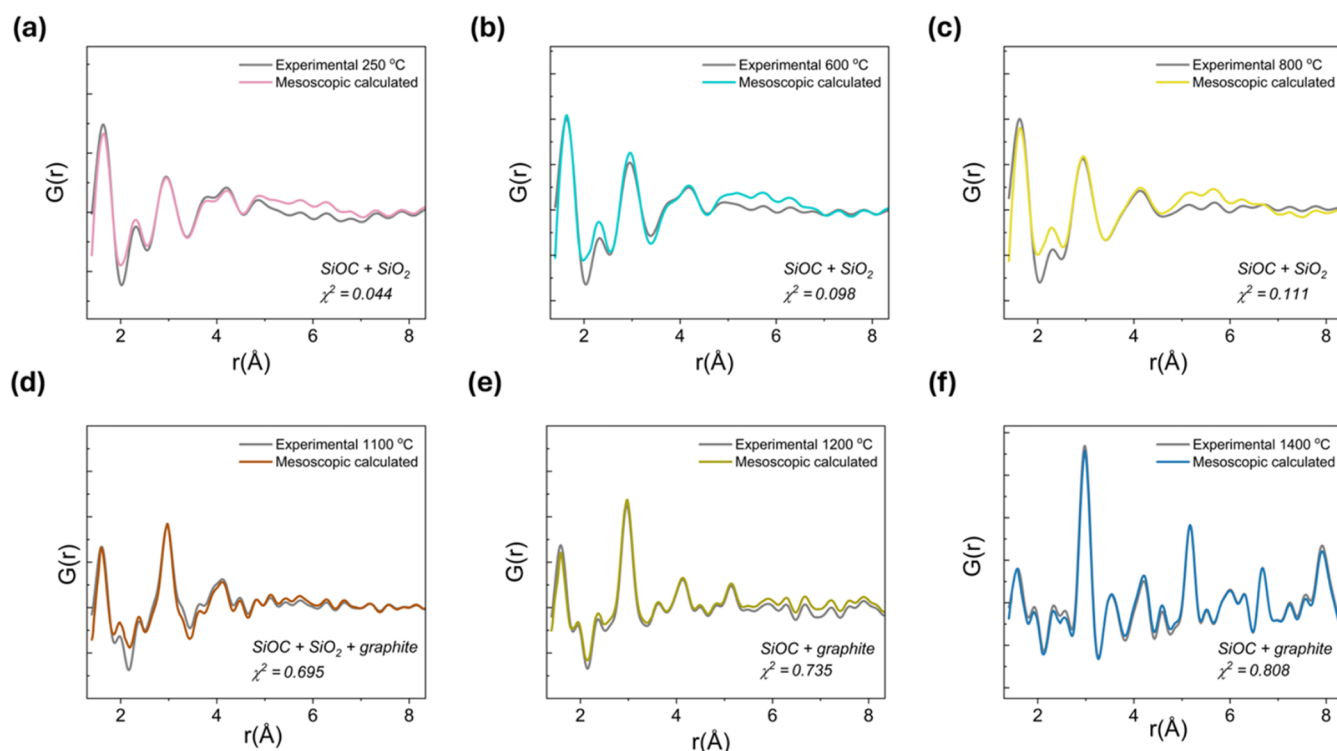
**Figure 3.** Resulting RMC fittings obtained from mesoscopic calculations of SPR-036 pyrolyzed at (a) 250 °C, (b) 600 °C, (c) 800 °C, (d) 1100 °C, (e) 1200 °C, and (f) 1400 °C, using a combination of SiOC, SiO$_2$, and graphite starting configurations depending on the processing temperature.
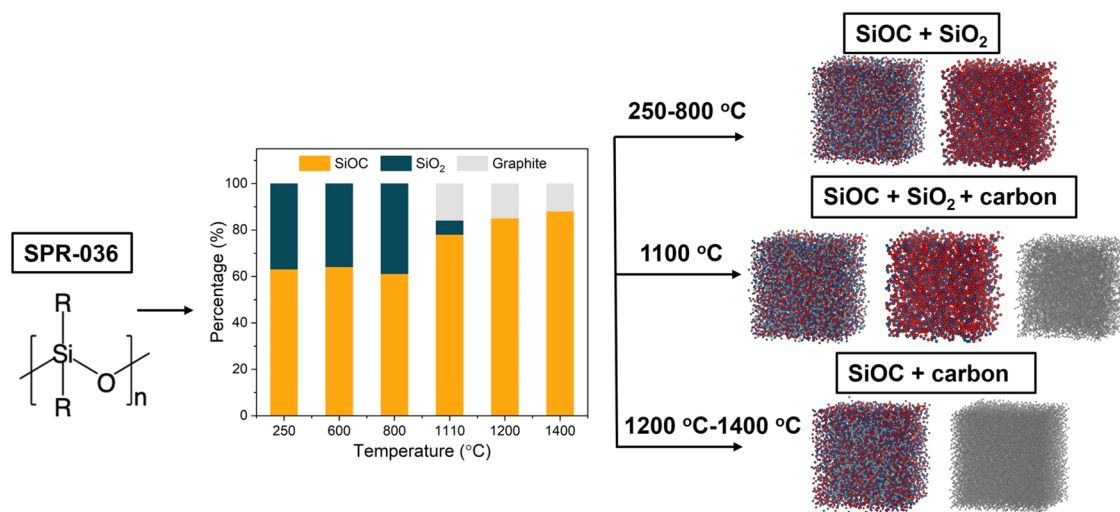


**Figure 4.** Summary of main phases detected in our RMC simulations of SPR-036-derived ceramics at different processing temperatures.

implemented in fullRMC to help evaluate how oxide or carbide-rich each material is for further heterogeneous modeling analysis.[30,39] The results are summarized in Table S2 and showcase a larger removal of C atoms at lower temperature, wherein O defects formation becomes more prevalent at temperatures above 1200 °C. While not a direct measure of stoichiometry, the associated C/O pairing with Si atoms in a forced SiOC local environment does showcase chemistry and structure evolving with temperature. Given these findings and the results of our XAS measurements, an additional SiO$_2$ phase was introduced to the RMC simulations of materials pyrolyzed at 250, 600, and 800 °C. While RMC fits using a single SiO$_2$ phase improves the fit of the first

coordination sphere (Figure S6), the misfit beyond 2.0 Å is notable. This suggests that while localized SiO$_2$ units are likely present at the being phase of the pyrolysis of SPR-036, their ordering has limited structural coherence.

Given the complexity of SiOC materials and the likelihood of localized phase separation, heterogeneous RMC modeling efforts were performed using the mesoscopic modeling function of fullRMC.[30,37] In mesoscopic modeling, different phases of materials can be modeled separately on the same set of PDF data, wherein the local structure and total contribute to combined PDF are modeled together.[37] This approach provides a more realistic understanding of the materials' structure through the modeling of multiple phases, avoiding

artifacts that could be captured using a single-phase material. Guided by our previous spectroscopy experiments, different heterogeneous modeling approaches were taken for SiOCs pyrolyzed at different temperatures. At lower temperatures (250–800 °C), a combination of SiOC and $SiO_2$ starting configurations were initially implemented, as shown in Figure 3(a–c). The incorporation of a $SiO_2$ model improved the fit agreement over a single-phase SiOC model (Figure S5(a–c), $\chi^2$ in Table S1), largely in the first coordination sphere. For SiOCs pyrolyzed at 1100, 1200, and 1400 °C, RMC simulations using a single-phase SiOC configuration still leads to slight misfitting of the first coordination sphere (Figure S5(d–f)). Insights from C K-edge NEXAFS and Raman spectroscopy indicate that a non-negligible presence of segregated carbon domains at these temperatures. While single graphitic phase expectedly does not accurately capture the experimental PDF alone (Figure S7), the first coordination sphere is relatively well captured, aligning with spectroscopy results. Given this temperature serving a possible transition from $SiO_2$ phase to SiOC and graphite, a ternary heterogeneous fit was performed using SiOC, graphite, and $SiO_2$ structure models. As shown in Figures 3d and S8, and Table S3, the ternary model improves the fit drastically, resulting in 78% SiOC contribution, 16% graphite, and 6% $SiO_2$ for materials pyrolyzed at 1100 °C. Materials pyrolyzed at 1200 and 1400 °C did not benefit from this ternary model approach, which is expected given the lack of Si–O-like features exhibited from the spectroscopic results for these materials. Instead, a binary graphite/SiOC model was chosen, which accurately captures the experimental PDF data (Figure 3(e,f), and Table S3). The results of the mesoscopic models are summarized in Figure 4, showcasing a trend of an SiOC network within a partial matrix of $SiO_2$ at lower pyrolysis temperature (<800 °C), which undergoes partial carbothermal reduction to a mixture of SiOC and graphite at higher temperatures.

It is important to note that attempts at including an SiC model in an analogous manner, either as a single phase or incorporated with the same phases used in our previous analysis, did not greatly improve the RMC fit. As such, the SiOC mixed phase tends to capture the local structure of SiC, which likely results in the SiC-like Bragg features observed in the HE-XRD patterns at higher temperature. These results align with recent work by Lu and Cheney, wherein an SiOC model was observed with an interpenetrating carbon network.[21]

To better understand the local structure of SiOC materials, the resulting RMC models were further evaluated in terms of local coordination numbers (CNs) and bond angle distributions, as summarized in Figures S9–S10 and Table S4. When considering contributions from SiOC phases, the local Si–O and Si–C CNs are effectively unchanged at a function of temperature, with a total coordination number below 4 that is roughly split between Si–O and Si–C contributions in this phase. Overall, this shows that Si–O/C units are thoroughly mixed and maintain an idealized coordination environment. This finding matches the expected Si–O and Si–C linkages in the starting polymer, along is somewhat contrasting against previous reports that suggest toward tetrahedral phase separation of $SiO_2$ and SiC domains.[19,74] We hypothesize that this is due to the differences in precursor and pyrolysis conditions used and/or the rigorous nature of our RMC analysis, wherein randomized Si–O and Si–C units can be evaluated locally around each Si atom. Bond angle distributions for Si–O–Si contributions for SiOCs range from as low as 140° to as high as 160°, with the uniformity of the distribution varying as a function of temperature. The average position of the distribution is ~153 to 160°, which is higher than the anticipated value of 144° for $SiO_2$[75] and align with local geometries found in amorphous silica.[75] The broad distribution of these Si–O–Si angles with notable deviations from the ideal tetrahedral shape confirms a distorted structure arrangement, which agrees well with our FTIR results as well, wherein the tightness of the distribution is slightly decreased with increasing temperature. In contrast, the distribution of Si–C–Si bond angles spanned a range of ~100 to ~165°, showcasing a broad distortion of the expected position at ~109° for tetrahedral Si–C units.[76,77] We hypothesize that the broader departure of ideal bond angle distribution behavior is a direct result of mixed Si–O/C local tetrahedral units, wherein the differences in local bond lengths due to the inclusion of O and C around Si.

## 4. CONCLUSIONS

Here, we used extensive synchrotron structure characterization to clarify the complexities of local Si–O–C formation in polymer-derived SiOCs. Both synchrotron scattering and spectroscopy methods yield insights into the predominantly amorphous nature of these materials. RMC simulations provide valuable insights into decoupling local Si–O and Si–C environments while confirming predominate heterogeneous phases in materials. Our combined analysis reveals that between 250 to 800 °C, the material consisted of amorphous SiOC and $SiO_2$. At 800 °C, a local crystallization of $SiO_2$ was initiated until 1100 °C, where SiOC manifest as SiC-like phases at higher temperature main phase. Further, it was shown that redistribution of carbon species in the SiOC network at 1100 °C leads to the formation of segregated carbon domains as well. At 1200 and 1300 °C, the SiOC phase begin to form, with polycrystalline SiOC evident at 1400 °C. Overall, the approach used in this study offers promising opportunities to investigate polymer-derived structures quantitatively and can address the limitations in characterizing amorphous and heterogeneous complex materials.

## ■ ASSOCIATED CONTENT

### Data Availability Statement

The data presented in this study are available from the corresponding author upon reasonable request.

### ⓢ Supporting Information

The Supporting Information is available free of charge at https://pubs.acs.org/doi/10.1021/acsomega.4c09094.

C K-edge analysis, Raman spectroscopy ATR-FTIR, HE-XRD, atomic PDFs, SiOC single-phase RMC models, $SiO_2$ single-phase RMC models, graphite single-phase RMC models, and bond angle distributions for all samples (PDF)

## ■ AUTHOR INFORMATION

### Corresponding Authors

**Matthew B. Dickerson** − *Materials and Manufacturing Directorate, Air Force Research Laboratory, Wright-Patterson AFB, Ohio 45433, United States;* ⓞ orcid.org/0000-0003-3000-0290; Email: matthew.dickerson.6@us.af.mil

**Timothy L. Pruyn** − *Materials and Manufacturing Directorate, Air Force Research Laboratory, Wright-Patterson AFB, Ohio 45433, United States*; Email: timothy.pruyn.1@us.af.mil

**Nicholas M. Bedford** − *School of Chemical Engineering, University of New South Wales, Sydney, New South Wales 2052, Australia; Department of Chemistry, Colorado School of Mines, Golden, Colorado 80401, United States*; orcid.org/0000-0002-4424-7094; Email: n.bedford@unsw.edu.au, nicholas.bedford@mines.edu

## Authors

**Haira G. Hackbarth** − *School of Chemical Engineering, University of New South Wales, Sydney, New South Wales 2052, Australia*; orcid.org/0000-0001-8995-4107

**Thomas S. Key** − *Materials and Manufacturing Directorate, Air Force Research Laboratory, Wright-Patterson AFB, Ohio 45433, United States*

**Taren Cataldo** − *School of Chemical Engineering, University of New South Wales, Sydney, New South Wales 2052, Australia*; orcid.org/0000-0002-2582-8555

**Ian Dillingham** − *Department of Chemistry, Johns Hopkins University, Baltimore, Maryland 21218, United States*; orcid.org/0009-0004-1696-8136

**Yuwei Yang** − *School of Chemical Engineering, University of New South Wales, Sydney, New South Wales 2052, Australia*

Complete contact information is available at:
https://pubs.acs.org/10.1021/acsomega.4c09094

## Notes

The authors declare no competing financial interest.

## REFERENCES

(1) Niu, M.; Wang, H.; Su, L.; Zhang, D.; Shi, J. Fabrication and properties of lightweight SiOC modified carbon-bonded carbon fiber composites. *Ceram. Int.* **2016**, *42* (9), 10614−10618.

(2) Silva, B. A.; Ribeiro, L. F. B.; González, S. Y. G.; Hotza, D.; de Fátima Peralta Muniz Moreira, R.; De Noni Junior, A. SiOC and SiCN-based ceramic supports for catalysts and photocatalysts. *Microporous Mesoporous Mater.* **2021**, *327*, No. 111435.

(3) Dong, B.; Han, Y.; Wang, T.; Lei, Z.; Chen, Y.; Wang, F.; Abadikhah, H.; Khan, S. A.; Hao, L.; Xu, X.; et al. Hard SiOC Microbeads as a High-Performance Lithium-Ion Battery Anode. *ACS Appl. Energy Mater.* **2020**, *3* (10), 10183−10191.

(4) Karakuscu, A.; Ponzoni, A.; Aravind, P. R.; Sberveglieri, G.; Soraru, G. D. Gas sensing behavior of mesoporous SiOC glasses. *J. Am. Ceram. Soc.* **2013**, *96* (8), 2366−2369.

(5) Zhuo, R.; Colombo, P.; Pantano, C.; Vogler, E. A. Silicon oxycarbide glasses for blood-contact applications. *Acta Biomater.* **2005**, *1* (5), 583−589.

(6) Vakifahmetoglu, C.; Presser, V.; Yeon, S.-H.; Colombo, P.; Gogotsi, Y. Enhanced hydrogen and methane gas storage of silicon oxycarbide derived carbon. *Microporous Mesoporous Mater.* **2011**, *144* (1), 105−112.

(7) Kleebe, H.-J.; Turquat, C.; Sorarù, G. D. Phase Separation in an SiCO Glass Studied by Transmission Electron Microscopy and Electron Energy-Loss Spectroscopy. *J. Am. Ceram. Soc.* **2001**, *84* (5), 1073−1080.

(8) Sorarù, G. D.; Karakuscu, A.; Boissiere, C.; Babonneau, F. On the shrinkage during pyrolysis of thin films and bulk components: The case of a hybrid silica gel precursor for SiOC glasses. *J. Eur. Ceram. Soc.* **2012**, *32* (3), 627−632.

(9) Hung, I.; Ionescu, E.; Sen, J.; Gan, Z.; Sen, S. Structure and Connectivity in an Amorphous Silicon Oxycarbide Polymer-Derived Ceramic: Results from 2D 29Si NMR Spectroscopy. *J. Phys. Chem. C* **2021**, *125* (8), 4777−4784.

(10) Stabler, C.; Roth, F.; Narisawa, M.; Schliephake, D.; Heilmaier, M.; Lauterbach, S.; Kleebe, H.-J.; Riedel, R.; Ionescu, E. High-temperature creep behavior of a SiOC glass ceramic free of segregated carbon. *J. Eur. Ceram. Soc.* **2016**, *36* (15), 3747−3753.

(11) Rosenburg, F.; Balke, B.; Nicoloso, N.; Riedel, R.; Ionescu, E. Effect of the Content and Ordering of the sp2 Free Carbon Phase on the Charge Carrier Transport in Polymer-Derived Silicon Oxy-carbides. *Molecules* **2020**, *25*, No. 5919, DOI: 10.3390/molecules25245919.

(12) Ackley, B. J.; Martin, K. L.; Key, T. S.; Clarkson, C. M.; Bowen, J. J.; Posey, N. D.; Ponder, J. F., Jr; Apostolov, Z. D.; Cinibulk, M. K.; Pruyn, T. L. Advances in the Synthesis of Preceramic Polymers for the Formation of Silicon-Based and Ultrahigh-Temperature Non-Oxide Ceramics. *Chem. Rev.* **2023**, *123* (8), 4188−4236.

(13) Stabler, C.; Ionescu, E.; Graczyk-Zajac, M.; Gonzalo-Juan, I.; Riedel, R. Silicon oxycarbide glasses and glass-ceramics: "All-Rounder" materials for advanced structural and functional applications. *J. Am. Ceram. Soc.* **2018**, *101* (11), 4817−4856.

(14) Bawane, K.; Erb, D.; Lu, K. Carbon content and pyrolysis atmosphere effects on phase development in SiOC systems. *J. Eur. Ceram. Soc.* **2019**, *39* (9), 2846−2854.

(15) Lu, K.; Li, J. Fundamental understanding of water vapor effect on SiOC evolution during pyrolysis. *J. Eur. Ceram. Soc.* **2016**, *36* (3), 411−422.

(16) Wang, L.; Lu, K.; Ma, R. Effects of different polymer precursors on the characteristics of SiOC bulk ceramics. *Appl. Phys. A* **2019**, *125* (6), No. 395.

(17) Hourlier, D.; Venkatachalam, S.; Ammar, M.-R.; Blum, Y. Pyrolytic conversion of organopolysiloxanes. *J. Anal. Appl. Pyrol.* **2017**, *123*, 296−306, DOI: 10.1016/j.jaap.2016.11.016.

(18) Kroll, P. Modeling the 'free carbon' phase in amorphous silicon oxycarbide. *J. Non-Cryst. Solids* **2005**, *351* (12), 1121−1126.

(19) Chaney, H.; Zhou, Y.; Lu, K. Understanding SiOC atomic structures via synchrotron X-ray and reactive force field potential studies. *Mater. Today Chem.* **2023**, *29*, No. 101429.

(20) Yang, N.; Ophus, C.; Savitzky, B. H.; Scott, M. C.; Bustillo, K.; Lu, K. Nanoscale characterization of crystalline and amorphous phases in silicon oxycarbide ceramics using 4D-STEM. *Mater. Charact.* **2021**, *181*, No. 111512.

(21) Lu, K.; Chaney, H. New insight into SiOC atomic structure evolution during early stage of pyrolysis. *J. Am. Ceram. Soc.* **2023**, *106* (5), 2737−2743.

(22) Brequel, H.; Soraru, G.; Schiffini, L.; Enzo, S. Radial distribution function of amorphous silicon oxycarbide compounds. *J. Metastable Nanocryst. Mater.* **2000**, *8*, 677−682, DOI: 10.4028/www.scientific.net/jmnm.8.677.

(23) Widgeon, S. J.; Sen, S.; Mera, G.; Ionescu, E.; Riedel, R.; Navrotsky, A. 29Si and 13C Solid-State NMR Spectroscopic Study of Nanometer-Scale Structure and Mass Fractal Characteristics of Amorphous Polymer Derived Silicon Oxycarbide Ceramics. *Chem. Mater.* **2010**, *22* (23), 6221−6228.

(24) Turquat, C.; Kleebe, H.-J.; Gregori, G.; Walter, S.; Sorarù, G. D. Transmission Electron Microscopy and Electron Energy-Loss Spectroscopy Study of Nonstoichiometric Silicon-Carbon-Oxygen Glasses. *J. Am. Ceram. Soc.* **2001**, *84* (10), 2189−2196.

(25) Saha, A.; Raj, R.; Williamson, D. L.; Kleebe, H. J. Characterization of Nanodomains in Polymer-Derived SiCN Ceramics Employing Multiple Techniques. *J. Am. Ceram. Soc.* **2005**, *88* (1), 232−234.

(26) Saha, A.; Raj, R.; Williamson, D. L. A Model for the Nanodomains in Polymer-Derived SiCO. *J. Am. Ceram. Soc.* **2006**, *89* (7), 2188−2195.

(27) Brequel, H.; Parmentier, J.; Sorar, G. D.; Schiffini, L.; Enzo, S. Study of the phase separation in amorphous silicon oxycarbide glasses under heat treatment. *Nanostruct. Mater.* **1999**, *11* (6), 721−731.

(28) Terban, M. W.; Billinge, S. J. L. Structural Analysis of Molecular Materials Using the Pair Distribution Function. *Chem. Rev.* **2022**, *122* (1), 1208−1272.

(29) Billinge, S. J. L. The rise of the X-ray atomic pair distribution function method: a series of fortunate events. *Philos. Trans. R. Soc., A* **2019**, *377* (2147), No. 20180413.

(30) Hackbarth, H. G.; Key, T. S.; Ackley, B. J.; Opletal, G.; Rawal, A.; Gallington, L.; Yang, Y.; Thomsen, L.; Dickerson, M. B.; Pruyn, T. L.; Bedford, N. M. Uncovering atomic-scale polymer-to-ceramic transformations in SiC polymer derived ceramics from polycarbosilanes. *J. Eur. Ceram. Soc.* **2024**, *44* (4), 1932−1945.

(31) Ferrari, A. C.; Robertson, J. Interpretation of Raman spectra of disordered and amorphous carbon. *Phys. Rev. B* **2000**, *61* (20), No. 14095.

(32) Ravel, B.; Newville, M. ATHENA, ARTEMIS, HEPHAESTUS: data analysis for X-ray absorption spectroscopy using IFEFFIT. *J. Synchrotron Radiat.* **2005**, *12* (4), 537−541.

(33) Gann, E.; McNeill, C. R.; Tadich, A.; Cowie, B. C. C.; Thomsen, L. Quick AS NEXAFS Tool (QANT): a program for NEXAFS loading and analysis developed at the Australian Synchrotron. *J. Synchrotron Radiat.* **2016**, *23* (1), 374−380.

(34) Hammersley, A. P. FIT2D: a multi-purpose data reduction, analysis and visualization program. *J. Appl. Crystallogr.* **2016**, *49* (2), 646−652.

(35) Juhás, P.; Davis, T.; Farrow, C. L.; Billinge, S. J. L. PDFgetX3: a rapid and highly automatable program for processing powder diffraction data into total scattering pair distribution functions. *J. Appl. Crystallogr.* **2013**, *46* (2), 560−566.

(36) FullRMC. accessed.

(37) Aoun, B. Stochastic atomic modeling and optimization with fullrmc. *J. Appl. Crystallogr.* **2022**, *55* (6), 1664−1676.

(38) Aoun, B. Fullrmc, a rigid body reverse monte carlo modeling package enabled with machine learning and artificial intelligence. *J. Comput. Chem.* **2016**, *37* (12), 1102−1111.

(39) Young, M. J.; Bedford, N. M.; Yanguas-Gil, A.; Letourneau, S.; Coile, M.; Mandia, D. J.; Aoun, B.; Cavanagh, A. S.; George, S. M.; Elam, J. W. Probing the Atomic-Scale Structure of Amorphous Aluminum Oxide Grown by Atomic Layer Deposition. *ACS Appl. Mater. Interfaces* **2020**, *12* (20), 22804−22814.

(40) Wyckoff, R. W. IX. Die Kristallstruktur von β-Cristobalit SiO2 (bei hohen Temperaturen stabile Form). 1925; Vol. 62 1−6, pp 189−200.

(41) Bragg, W. L. The structure of some crystals as indicated by their diffraction of X-rays. *Proc. R. Soc. London, Ser. A* **1913**, *89* (610), 248−277.

(42) Stukowski, A. Visualization and analysis of atomistic simulation data with OVITO−the Open Visualization Tool. *Modell. Simul. Mater. Sci. Eng.* **2010**, *18* (1), No. 015012.

(43) Liu, P.; Irmak, E. A.; De Backer, A.; De wael, A.; Lobato, I.; Béché, A.; Van Aert, S.; Bals, S. Three-dimensional atomic structure of supported Au nanoparticles at high temperature. *Nanoscale* **2021**, *13* (3), 1770−1776.

(44) Le Roux, S.; Petkov, V.; Le, S. ISAACS—Interactive structure analysis of amorphous and crystalline systems. *J. Appl. Cryst.* **2010**, *43*, 181−185.

(45) d'Eril, M. M.; Zambotti, A.; Graczyk-Zajac, M.; Ionescu, E.; Soraru, G. D.; Riedel, R. Effect of ultra-fast pyrolysis on polymer-derived SiOC aerogels and their application as anodes for Na-ion batteries. *Open Ceram.* **2023**, *14*, No. 100354.

(46) Soraru, G. D.; Tavonatti, C.; Kundanati, L.; Pugno, N.; Biesuz, M. Effect of the pyrolysis atmosphere on the mechanical properties of polymer-derived SiOC and SiCN. *J. Am. Ceram. Soc.* **2020**, *103* (11), 6519−6530.

(47) Okoroanyanwu, U.; Bhardwaj, A.; Einck, V.; Ribbe, A.; Hu, W.; Rodriguez, J. M.; Schmidt, W. R.; Watkins, J. J. Rapid Preparation and Electrochemical Energy Storage Applications of Silicon Carbide and Silicon Oxycarbide Ceramic/Carbon Nanocomposites Derived Via Flash Photothermal Pyrolysis of Organosilicon Preceramic Polymers. *Chem. Mater.* **2021**, *33* (2), 678−694.

(48) Zambotti, A.; Valentini, F.; Lodi, E.; Pegoretti, A.; Tyrpekl, V.; Kohúteková, S.; Soraru, G. D.; Kloda, M.; Biesuz, M. Thermochemical heat storage performances of magnesium sulphate confined in polymer-derived SiOC aerogels. *J. Alloys Compd.* **2022**, *895*, No. 162592.

(49) Liu, L.; Yiu, Y. M.; Sham, T. K.; Zhang, L.; Zhang, Y. Electronic Structures and Optical Properties of 6H- and 3C-SiC Microstructures and Nanostructures from X-ray Absorption Fine Structures, X-ray Excited Optical Luminescence, and Theoretical Studies. *J. Phys. Chem. C* **2010**, *114* (15), 6966−6975.

(50) Morresi, T.; Timpel, M.; Pedrielli, A.; Garberoglio, G.; Tatti, R.; Verucchi, R.; Pasquali, L.; Pugno, N. M.; Nardi, M. V.; Taioli, S. A novel combined experimental and multiscale theoretical approach to unravel the structure of SiC/SiOx core/shell nanowires for their optimal design. *Nanoscale* **2018**, *10* (28), 13449−13461.

(51) Kanda, K.; Suzuki, S.; Niibe, M.; Hasegawa, T.; Suzuki, T.; Saitoh, H. Local Structure Analysis on Si-Containing DLC Films Based on the Measurement of C K-Edge and Si K-Edge X-ray Absorption Spectra. *Coatings* **2020**, *10* (4), No. 330.

(52) Chaboy, J.; Barranco, A.; Yanguas-Gil, A.; Yubero, F.; González-Elipe, A. R. Si K-edge XANES study of Si O x C y H z amorphous polymeric materials. *Phys. Rev. B* **2007**, *75* (7), No. 075205.

(53) Kohn, S.; Hoffbauer, W.; Jansen, M.; Franke, R.; Bender, S. Evidence for the formation of SiON glasses. *J. Non-Cryst. Solids* **1998**, *224* (3), 232−243.

(54) Bobrin, V. A.; Hackbarth, H. G.; Yao, Y.; Bedford, N. M.; Zhang, J.; Corrigan, N.; Boyer, C. Customized Nanostructured Ceramics via Microphase Separation 3D Printing. *Adv. Sci.* **2023**, *10* (n/a), No. 2304734.

(55) Narisawa, M.; Hokazono, H.; Mitsuhara, K.; Inoue, H.; Ohta, T. Structure and properties of white Si−O−C (−H) ceramics derived from polycarbosilane by thermal oxidation curing and H2 decarbonization process. *J. Ceram. Soc. Jpn.* **2016**, *124* (10), 1094−1099.

(56) Nimmo, J. P., II; Kroll, P. First-Principles Calculations and Analysis of 29Si Nuclear Magnetic Resonance Chemical Shifts in Silicon Oxycarbide Ceramics. *J. Phys. Chem. C* **2014**, *118* (51), 29952−29961.

(57) Lan, X.; Li, Y.; Wang, Z. High-temperature electromagnetic wave absorption, mechanical and thermal insulation properties of in-situ grown SiC on porous SiC skeleton. *Chem. Eng. J.* **2020**, *397*, No. 125250.

(58) Espinal, L.; Green, M. L.; Fischer, D. A.; DeLongchamp, D. M.; Jaye, C.; Horn, J. C.; Sakwa-Novak, M. A.; Chaikittisilp, W.; Brunelli, N. A.; Jones, C. W. Interrogating the Carbon and Oxygen K-Edge NEXAFS of a CO2-Dosed Hyperbranched Aminosilica. *J. Phys. Chem. Lett.* **2015**, *6* (1), 148−152.

(59) Pan, J.; Ren, J.; Xie, Y.; Wei, X.; Guan, Y.; Yan, X.; Tang, H.; Cheng, X. Porous SiOC composites fabricated from preceramic polymers and wood powders for efficient dye adsorption and removal. *Res. Chem. Intermed.* **2017**, *43* (7), 3813−3832.

(60) Lu, K.; Erb, D.; Bawane, K.; Yang, N. Comparison of traditional and flash pyrolysis of different carbon content silicon oxycarbides. *J. Eur. Ceram. Soc.* **2019**, *39* (10), 3035−3041.

(61) Rosenburg, F.; Ionescu, E.; Nicoloso, N.; Riedel, R. High-temperature Raman spectroscopy of nano-crystalline carbon in silicon oxycarbide. *Materials* **2018**, *11* (1), No. 93.

(62) Mera, G.; Navrotsky, A.; Sen, S.; Kleebe, H.-J.; Riedel, R. Polymer-derived SiCN and SiOC ceramics−structure and energetics at the nanoscale. *J. Mater. Chem. A* **2013**, *1* (12), 3826−3836, DOI: 10.1039/c2ta00727d.

(63) Liu, X.; Zhang, H.; Liu, C.; Guo, H.; Xia, K. Phenol Adsorption Performance of Nitrogen-Doped Porous Carbon Derived from Silicon Oxycarbide Ceramics. *Silicon* **2024**, *16* (4), 1743−1752.

(64) Santhosh, B.; Vakifahmetoglu, C.; Ionescu, E.; Reitz, A.; Albert, B.; Sorarù, G. D. Processing and thermal characterization of polymer derived SiCN(O) and SiOC reticulated foams. *Ceram. Int.* **2020**, *46* (5), 5594−5601.

(65) Su, Q.; King, S.; Li, L.; Wang, T.; Gigax, J.; Shao, L.; Lanford, W. A.; Nastasi, M. Microstructure-mechanical properties correlation in irradiated amorphous SiOC. *Scr. Mater.* **2018**, *146*, 316−320.

(66) Loughney, P. A.; Cuillier, P.; Pruyn, T. L.; Doan-Nguyen, V. Tracking copper nanofiller evolution in polysiloxane during processing into SiOC ceramic. *J. Appl. Crystallogr.* **2024**, *57* (4), 945−954.

(67) Mizuguchi, S.; Inoue, S.; Ishimaru, M.; Su, Q.; Nastasi, M. Compositional effects on radiation tolerance of amorphous silicon oxycarbide. *J. Nucl. Mater.* **2019**, *518*, 241−246.

(68) Lee, S.; Xu, H. Using powder XRD and pair distribution function to determine anisotropic atomic displacement parameters of orthorhombic tridymite and tetragonal cristobalite. *Acta Crystallogr., Sect. B:Struct. Sci., Cryst. Eng. Mater.* **2019**, *75*, 160−167.

(69) Niu, M.; Jayanthi, K.; Gao, H.; Solomon, A. P.; O'Quinn, E. C.; Su, L.; Qin, Y.; Toimil-Molares, M. E.; Wang, H.; Lang, M.; Navrotsky, A. Structural and thermodynamic evolution of an amorphous SiOC ceramic after swift heavy ion irradiation. *Acta Mater.* **2023**, *242*, No. 118475.

(70) Su, Q.; Inoue, S.; Ishimaru, M.; Gigax, J.; Wang, T.; Ding, H.; Demkowicz, M. J.; Shao, L.; Nastasi, M. Helium irradiation and implantation effects on the structure of amorphous silicon oxycarbide. *Sci. Rep.* **2017**, *7* (1), No. 3900.

(71) Bai, W.; Widgeon, S.; Sen, S. Structure and topological characteristics of amorphous silicon oxycarbide networks: Results from Reverse Monte Carlo simulations. *J. Non-Cryst. Solids* **2014**, *386*, 29−33.

(72) Lin, X.; Wang, C. G.; Yu, M. J.; Lin, Z. T.; Zhang, S. Study on the Local Structure of PAN-Based Carbon Fiber Using Radial Distribution Function Based on XRD. *Adv. Mater. Res.* **2013**, *664*, 614−619, DOI: 10.4028/www.scientific.net/amr.664.614.

(73) Biswas, P.; Atta-Fynn, R.; Drabold, D. A. Reverse Monte Carlo modeling of amorphous silicon. *Phys. Rev. B* **2004**, *69* (19), No. 195207.

(74) Kleebe, H.-J.; Blum, Y. D. SiOC ceramic with high excess free carbon. *J. Eur. Ceram. Soc.* **2008**, *28* (5), 1037−1042.

(75) Wright, A. C. Neutron scattering from vitreous silica. V. The structure of vitreous silica: What have we learned from 60 years of diffraction studies? *J. Non-Cryst. Solids* **1994**, *179*, 84−115.

(76) Gao, F.; Weber, W. J. Computer simulation of disordering and amorphization by Si and Au recoils in 3C−SiC. *J. Appl. Phys.* **2001**, *89* (8), 4275−4281.

(77) Rino, J. P.; Ebbsjö, I.; Branicio, P. S.; Kalia, R. K.; Nakano, A.; Shimojo, F.; Vashishta, P. Short- and intermediate-range structural correlations in amorphous silicon carbide: A molecular dynamics study. *Phys. Rev. B* **2004**, *70* (4), No. 045207.